International Journal of Biological Macromolecules 239 (2023) 124258

Contents lists available at ScienceDirect

International Journal of Biological Macromolecules

journal homepage: www.elsevier.com/locate/ijbiomac

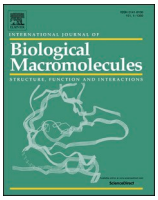

Lignin-enriched tricalcium phosphate/sodium alginate 3D scaffolds for application in bone tissue regeneration

A.S. Silva-Barroso [a,1], Cátia S.D. Cabral [a,1], Paula Ferreira [b,c], André F. Moreira [a,d], Ilídio J. Correia [a,*]

[a] CICS-UBI—Centro de Investigação em Ciências da Saúde, Universidade da Beira Interior, Av. Infante D. Henrique, 6200-506 Covilhã, Portugal
[b] CIEPQPF–Departamento de Engenharia Química, Universidade de Coimbra, Rua Silvio Lima, 3030-790 Coimbra, Portugal
[c] Instituto Superior de Engenharia de Coimbra, Instituto Politécnico de Coimbra, Rua Pedro Nunes, 3030-199 Coimbra, Portugal
[d] CPIRN-UDI/IPG–Center of Potential and Innovation in Natural Resources, Research Unit for Inland Development, Instituto Politécnico da Guarda, Avenida Dr. Francisco de Sá Carneiro, 6300-559 Guarda, Portugal

ARTICLE INFO

Keywords:
3D scaffolds
Bone regeneration
Composite materials
Lignin
Rapid prototyping

ABSTRACT

The bone is a connective, vascularized, and mineralized tissue that confers protection to organs, and participates in the support and locomotion of the human body, maintenance of homeostasis, as well as in hematopoiesis. However, throughout the lifetime, bone defects may arise due to traumas (mechanical fractures), diseases, and/or aging, which when too extensive compromise the ability of the bone to self-regenerate. To surpass such clinical situation, different therapeutic approaches have been pursued. Rapid prototyping techniques using composite materials (consisting of ceramics and polymers) have been used to produce customized 3D structures with osteoinductive and osteoconductive properties. In order to reinforce the mechanical and osteogenic properties of these 3D structures, herein, a new 3D scaffold was produced through the layer-by-layer deposition of a tricalcium phosphate (TCP), sodium alginate (SA), and lignin (LG) mixture using the Fab@Home 3D-Plotter. Three different TCP/LG/SA formulations, LG/SA ratio 1:3, 1:2, or 1:1, were produced and subsequently evaluated to determine their suitability for bone regeneration. The physicochemical assays demonstrated that the LG inclusion improved the mechanical resistance of the scaffolds, particularly in the 1:2 ratio, since a 15 % increase in the mechanical strength was observed. Moreover, all TCP/LG/SA formulations showed an enhanced wettability and maintained their capacity to promote the osteoblasts' adhesion and proliferation as well as their bioactivity (formation of hydroxyapatite crystals). Such results support the LG inclusion and application in the development of 3D scaffolds aimed for bone regeneration.

1. Introduction

Bone is a connective, vascularized, and mineralized tissue that is under constant remodeling throughout human life and is enrolled in different functions such as organ protection, locomotion, maintenance of body homeostasis, and hematopoiesis [1–3]. Despite the self-regenerative capacity of bone, when the damage is too extensive, the structure of the bone can be compromised. On these occasions, the gold standard treatments used in the clinic rely on the application of autografts, allografts, or xenografts. However, these approaches have some disadvantages such as the limited availability, the formation of new lesions, and the possibility of immune rejection [4–6]. Thus, new approaches are currently being developed, based on the use of biomaterials and tissue engineering, for application in bone injuries [7–10].

Rapid prototyping techniques allow the production of customized 3D structures exhibiting osteoinductive and osteoconductive properties [11]. Furthermore, the available state of art technologies are compatible with the combination of different materials, inorganic and organic, as well as the immediate incorporation of cells to accelerate the bone regeneration process [12]. The composite 3D structures developed so far, are aimed to reproduce the native extracellular matrix of the bone: an inorganic phase composed mainly of calcium phosphate crystals in the form of hydroxyapatite, and an organic matrix mostly composed of type I collagen fibrils [13,14]. In this way, researchers aggregate the

* Corresponding author.
E-mail address: icorreia@ubi.pt (I.J. Correia).
[1] The authors contributed equally to the manuscript.

https://doi.org/10.1016/j.ijbiomac.2023.124258
Received 18 January 2023; Received in revised form 17 March 2023; Accepted 27 March 2023
Available online 31 March 2023

enhanced mechanical properties of ceramics, such as hydroxyapatite, tricalcium phosphate (TCP), and glass ceramics, with the bioactivity and biocompatibility of polymers (*e.g.*, collagen, alginate, chitosan, and gelatin) to create supporting matrices that stimulate the bone tissue formation [15,16]. However, up to now the natural polymers used in these composite formulations still lead to poor performances *in vivo*, presenting suboptimal mechanical and physicochemical properties [16].

In the present work, a novel 3D scaffold was produced by the layer-by-layer deposition of a mixture composed of tricalcium phosphate (TCP), sodium alginate (SA), and lignin (LG) using the Fab@Home 3D-Plotter printer. TCP is a resorbable calcium/phosphate ceramic with high similarity to the minerals found in the native bone matrix [17]. Moreover, this ceramic is also highly biocompatible and osteoconductive [18]. In turn, SA is a natural, biocompatible, hydrophilic polymer with high viscosity in contact with water that is obtained from the cell walls of brown seaweed [19]. Additionally, SA-based materials can undergo ionotropic crosslinking in the presence of bivalent cations (*e.g.*, Ca^{2+}), which can be explored to further reticulate the scaffold after the bioprinting process [20,21]. Particularly, in 3D printing approaches, this tunable viscoelasticity is explored to achieve injectable formulations capable of maintaining, with great fidelity, the original printed pattern. Nevertheless, the SA lacks the mechanical resistance necessary in bone tissue applications. LG is a natural polymer with a complex and branched structure that originates from phenylpropanes and monolignols [22]. This material is found in plant tissues, where it is responsible for conferring rigidity and shape to the plant cells, being the second most abundant organic material after cellulose [23,24]. Different processing methods can be used to obtain various types of lignin, such as kraft, organosolv, soda lignins, and lignosulphonates, that differ in molecular weight and constitution [25]. Such has been the main shortcoming for the application of LG in biomedicine. Nevertheless, LG presents unique properties, *i.e.*, stability, biocompatibility, and mechanical resistance, as well as the capacity to protect against oxidative stress and UV light, that are interesting for biomedical applications [26–30]. Herein, LG was incorporated, for the first time, in the TCP/SA mixture, at a ratio of LG and SA (1:3, 1:2, and 1:1), in order to evaluate its impact on the physicochemical, mechanical, and biological properties of 3D scaffolds produced by rapid prototyping and aimed to be used in bone tissue regeneration.

2. Materials and methods

2.1. Materials

Alizarin Red S (ARS), Dulbecco's modified Eagle's medium (DMEM-F12), ethylenediaminetetraacetic acid (EDTA), diethanolamine, glutaraldehyde 2.5 % (v/v), hydrochloric acid (HCl), kraft lignin (Product Number: 471003; Manufacture: Biological extraction; Pine Trees; ≈ 10,000 g/mol, impurities ≤3.6 % sulfur), phosphate buffered saline solution (PBS), di-potassium hydrogen phosphate trihydrate (HK_2O_4.P.$3H_2O$), resazurin, *p*-Nitrophenylphosphate (pNPP), sodium alginate (Product Number: W201502; Manufacture: Chemical; Viscosity: 5–40 cPs at 1 % in water), sodium hydroxide (NaOH), Triton X-100, and trypsin were purchased from Sigma-Aldrich (Sintra, Portugal). Normal human osteoblast (hOB; 406-05f) cells were bought from Cell Applications, Inc. (San Diego, USA). Fetal bovine serum was provided by Biochrom AG (Berlin, Germany). Calcium chloride ($CaCl_2$), sodium chloride (NaCl), Tris-buffered saline (TBS), and L-Ascorbic acid (LAA) were obtained from Fisher Scientific (Porto Salvo, Portugal). Tricalcium phosphate (TCP) was purchased from Panreac (Barcelona, Spain). Sodium bicarbonate ($NaHCO_3$) was obtained from Labchem (Santo Antão do Tojal, Portugal). Magnesium chloride hexahydrate ($MgCl_2.6H_2O$), potassium chloride (KCl), and sodium sulfate anhydrous (Na_2SO_4) were purchased from Labkem (Barcelona, Spain). Propidium Iodide buffer was acquired from Life Technologies (Maryland, USA). Calcein AM was supplied by Calbiochem (Merck Millipore, Oeiras, Portugal). Ethanol 99.5 % (EtOH) was obtained from Aga (Prior Velho, Portugal). Double deionized and filtered water was obtained using a Milli-Q Advantage A10 ultrapure Water Purification System (0.22 μm filtered; 18.2 MΩ/cm at 25 °C).

Table 1
General composition of the TCP/LG/SA and TCP/SA scaffolds.

	Scaffolds			
	TCP/LG/SA			TCP/SA
LG/SA ratio	1:3	1:2	1:1	–
TCP (g)	6	6	6	6
SA (g)	1.125	1	0.75	1.5
LG (g)	0.375	0.5	0.75	–
Density (g/mL)	0.75			

2.2. Methods

2.2.1. Production of scaffolds

The different 3D scaffolds were prepared by varying the LG/SA ratio, according to Table 1. For that purpose, the SA and LG were sequentially dissolved in double deionized and filtered water and homogenized using an X10/25 Ultra-turrax for 35 min. Subsequently, the TCP content was added to the polymeric mixture and homogenized for 20 min. The prepared TCP/LG/SA mixture was then loaded into a syringe (10 mL Luer Lock) and extruded using the Fab@Home 3D printer. The printing process started with the conversion of the CAD file to STL. Then, different parameters were defined in the Fab@home v0.23 software (Table S1) and the 3D TCP/LG/SA scaffolds were obtained through a layer-by-layer fabrication process. After the printing process, the scaffolds were immersed in a 5 % $CaCl_2$ (w/v) solution for 24 h to achieve the full crosslinking of the SA chains, both in the scaffolds' exterior and interior. Afterward, the scaffolds were removed from the $CaCl_2$ solution and dried at 37 °C for 3 days.

2.2.2. Characterization of the morphology of the 3D scaffolds

The scaffolds' morphology, surface, and macroporosity were characterized using Scanning Electron Microscopy (SEM). For this purpose, the samples were mounted on aluminium stubs, using araldite glue, and coated with gold, using a Quorum Q150RES sputter coater (Quorum Technologies, UK). Then, the scaffolds' images at different magnifications were acquired in a Hitachi S-3400N scanning electron microscope (Japan) operated at an accelerating voltage of 20 kV.

2.2.3. Characterization of the scaffolds' physicochemical properties

2.2.3.1. Attenuated Total reflectance- Fourier transform infrared spectroscopy. Attenuated Total Reflectance Fourier Transform Infrared (ATR-FTIR) spectroscopy was used to characterize the chemical composition of the scaffolds. Spectra were acquired with an average of 128 scans, with a spectral resolution of 32 cm^{-1} and a range of 400–4000 cm^{-1} [31]. The scaffolds were crushed into powder and then mounted on a diamond window in order to allow the samples' analysis using the Nicolet iS10 FTIR Spectrophotometer (Thermo Scientific, Waltham, MA, USA). For comparison purposes, all the raw materials used in the production of the scaffolds were analyzed in their pure state.

2.2.3.2. Energy-dispersive spectroscopic analysis. Energy-Dispersive Spectroscopy (EDS) was used to determine the elemental composition of the 3D scaffolds as well as the surface modifications during the mineralization process. Briefly, the samples were placed on aluminium stubs, air-dried at room temperature (RT), and then analyzed in an XFlash Detector 5010 (Bruker Nano, Germany).

2.2.4. Characterization of the scaffolds' mechanical properties

The mechanical properties of the scaffolds ($n = 5$) were analyzed in

dry and wet conditions. To mimic physiological conditions, wet scaffolds were immersed overnight in the standard simulated body fluid (SBF). The SBF solution has almost identical ion concentrations as the human blood plasma (142.0 mM Na^+, 5 mM K^+, 1.5 mM Mg^{2+}, 2.5 mM Ca^{2+}, 147.8 mM Cl^-, 4.2 mM HCO_3^-, 1.0 mM HPO_4^{2-} and 0.5 mM SO_4^{2-}) at a pH of 7.4. This solution was prepared using a protocol previously described in the literature [32]. Then, the samples were subjected to compression tests for evaluating the mechanical behavior of the scaffolds. The samples' testing was performed at RT using a Shimadzu AG-X tensile testing machine (Tokyo, Japan) with a load cell of 5 kN and a cruising speed of 2 mm/min.

The compressive strength (*Cs*) was calculated using Eq. (1) [33]:

$$Cs = \frac{F}{w \times l} \quad (1)$$

Where *F* represents the load at the time of fracture, *w* and *l* correspond to the width and length of the scaffolds, respectively.

Young's modulus (*YM*) was also calculated using the stress-strain relationship, shown in Eq. (2) [33]:

$$YM = \frac{Cs}{(dL/L)} \quad (2)$$

Where *Cs* corresponds to the scaffold's compressive strength, *dL* refers to the elongation or compression (*i.e.* change in length) and *L* corresponds to the length of the scaffold.

2.2.5. Characterization of the scaffolds' swelling profile

The scaffolds' swelling capacity was evaluated using a method previously described in the literature [34]. Briefly, scaffolds ($n = 5$) were immersed in Tris-buffered saline (TBS) solution (1×, pH 7.4) and incubated under stirring (60 rpm) at 37 °C for ≈ 3 days. At predetermined time intervals, the scaffolds were recovered by removing the fluid excess, weighed, and re-immersed in the TBS solution. The swelling was then calculated using Eq. (3):

$$Swelling\ (\%) = \left(\frac{W_t - W_o}{W_o}\right) \times 100 \quad (3)$$

Where W_t indicates the final weight of the scaffolds, and W_o refers to the initial weight.

2.2.6. Contact angle measurements

The scaffolds' hydrophilicity was characterized using the sessile drop method of water contact angle (WCA) measurement. For that purpose, a drop of deionized water (10 μL) was automatically dispersed onto the sample's surface and the resultant contact angle was assessed using a Dataphysics OCA 20 contact angle analyzer (Dataphysics Instruments, Filderstadt, Germany). Ten measurements on several points of the scaffolds' surface were performed in order to determine the mean static contact angle.

2.2.7. Evaluation of scaffolds' porosity

The total porosity of the scaffolds was evaluated using a liquid displacement method, as previously described elsewhere [33]. Initially, the scaffolds were weighed and then immersed in absolute ethanol (EtOH) for 48 h. After this period, the samples were weighed again. EtOH was chosen because of its ability to penetrate the structure of the scaffolds without generating structural changes, *i.e.*, swelling or shrinkage [35]. The scaffolds' porosity was calculated using Eq. (4):

$$Porosity\ (\%) = \frac{W_w - W_d}{D_{EtOH} \times V_{scaffold}} \times 100 \quad (4)$$

Where W_w and W_d correspond to the final and initial scaffold's weight of the scaffold, respectively. D_{EtOH} refers to the EtOH density at RT and the $V_{scaffold}$ corresponds to the scaffolds' volume.

2.2.8. Characterization of the biodegradation profile of the scaffolds

The scaffolds' degradation profile was evaluated in the absence or presence of lysozyme. For that purpose, the scaffolds were incubated in DMEM-F12 medium (with or without lysozyme), at 37 °C, under agitation (60 rpm) [36,37]. At predetermined intervals, the scaffolds were removed from the solution, frozen at 80 °C, freeze-dried for 3 h, and weighed. The weight loss percentage at each timepoint was determined using Eq. (5):

$$Weight\ loss\ (\%) = \left(\frac{W_i - W_f}{W_i}\right) \times 100 \quad (5)$$

Where W_i refer to the initial weight of the scaffold and W_f represents the weight of the scaffolds at time t.

2.2.9. Characterization of the scaffolds' biological properties

2.2.9.1. Evaluation of the scaffolds' effect on the viability and proliferation of hOB cells. The scaffolds' cytotoxic profile was evaluated on hOB cells using the resazurin assay [37]. Initially, the produced scaffolds were cut into small pieces, deposited in 96-well plates, and sterilized by ultraviolet radiation for 1 h. Subsequently, 10×10^3 cells/well were seeded in contact with the samples and incubated for 1, 3, and 7 days. At the predetermined times, the medium was removed, and the cells were incubated with 110 μL of fresh medium containing resazurin (10 μL) for 4 h in the dark (37 °C, 5 % CO_2). Then, the resorufin fluorescence was measured ($\lambda_{ex} = 560$ nm and $\lambda_{em} = 590$ nm) using a Spectramax Gemini EM spectrofluorometer (Molecular Devices LLC, CA, USA). Cells incubated without materials and cells incubated with EtOH (70 %) were used as negative (K^-) and positive (K^+) controls, respectively. Furthermore, live/dead confocal experiments were also performed to confirm the cytocompatibility of TCP/LG/SA and TCP/SA scaffolds. Briefly, hOB cells were seeded on μ-Slide 8-well Ibidi imaging plates (Ibidi GmbH) and exposed to the different materials for 1 and 3 days. Then, the live and dead cells were stained with Calcein AM and propidium iodide (PI), respectively, and the images were obtained using a Zeiss LSM 710 confocal microscope.

2.2.9.2. Characterization of cell adhesion at the surface of the scaffolds. SEM was used to evaluate the cell adhesion on the surface of the scaffolds. For this purpose, hOB cells were seeded on the scaffolds and incubated for 1, 3, and 7 days. Afterward, the scaffolds with cells on their surface were fixed, at predetermined timepoints, with glutaraldehyde (2.5 % (v/v)) for 30 min. Subsequently, the samples were frozen at −80 °C, freeze-dried for 3 h, and finally analyzed by SEM (as described in Section 2.2.2).

2.2.9.3. Mineralization in a model medium. The mineralization at the scaffolds' surface was evaluated upon immersion in SBF solution (prepared as described in Section 2.2.4) at 37 °C, for 7 and 21 days [32]. At the predetermined intervals, the scaffolds were removed from the SBF solution, dried and, subsequently, the deposition of calcium and phosphate ions as well as the presence of apatite layers on scaffolds' surface was screened using SEM.

Alizarin Red S (ARS) staining was also used to study the scaffolds' ability to stimulate hOB cells to accumulate calcium, using a previously optimized protocol [38]. Briefly, hOB cells were grown for 1, 3, 7, and 14 days in the presence of the scaffolds. Afterward, samples were fixed with formaldehyde (4 % (v/v)) for 1 h and stained with ARS (1 mL, 40 mM, pH = 4.1–2.3). Then, the samples were washed with deionized water, to remove ARS excess, and the calcium deposits were quantified by measuring the ARS absorbance. For that purpose, samples were incubated under stirring with acetic acid (1 mL; 10 % (v/v)) for 30 min, vortexed for 30 s, and heated to 85 °C, for 10 min. Subsequently, the samples were centrifuged (14,000 *g*, 25 min, RT) and the supernatant was neutralized with ammonium hydroxide (200 μL; 10 % (v/v)).

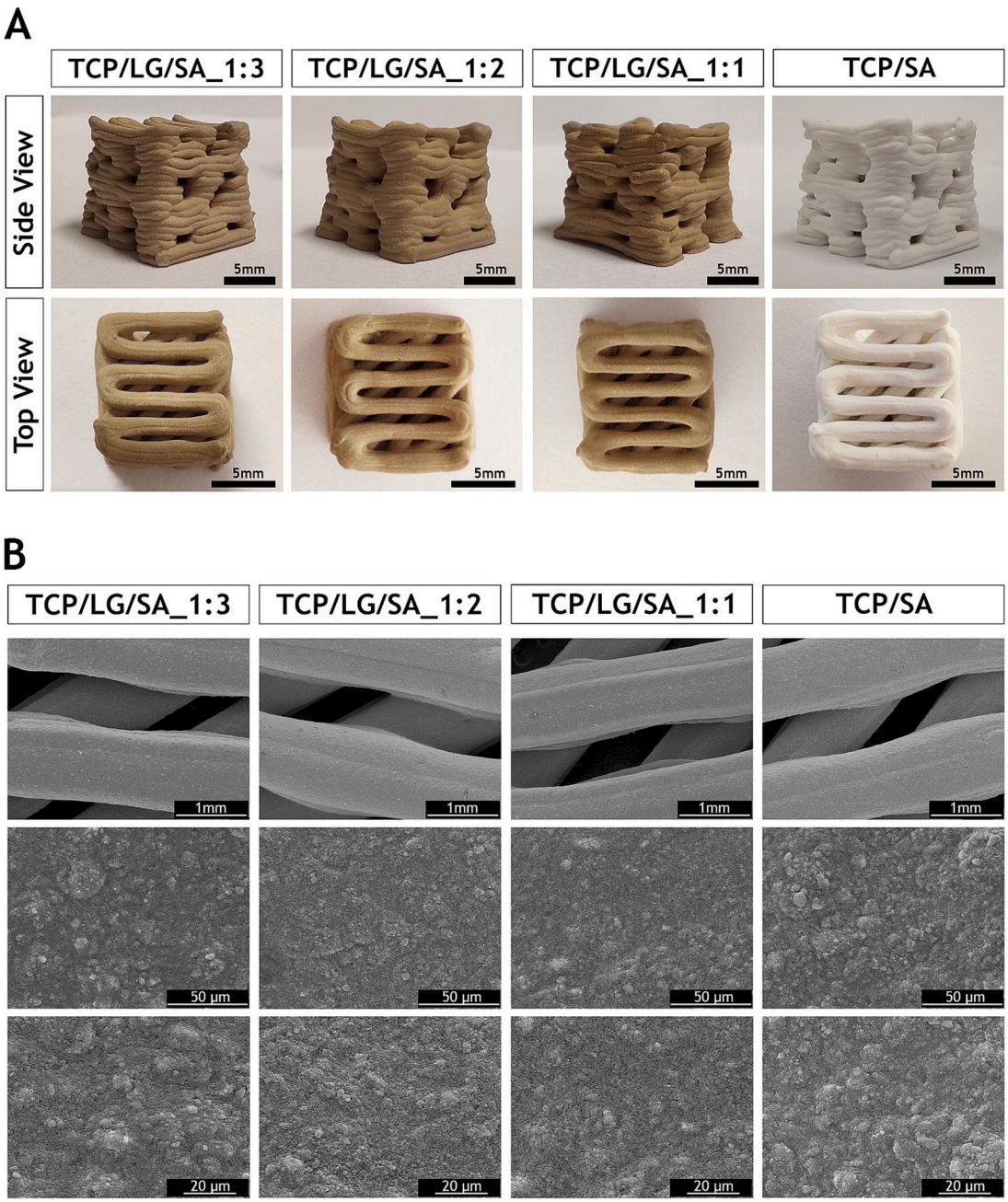

Fig. 1. Representative macroscopic images of the different scaffolds produced (side and top views) (A), and SEM images showing the morphology and surface topography of the 3D scaffolds produced at different magnifications (B).

Finally, the samples' absorption was read at 405 nm using a Biorad xMark microplate spectrophotometer. Additionally, a calibration curve for ARS was also performed for quantification purposes.

2.2.9.4. Evaluation of the alkaline phosphatase (ALP) activity. The ALP activity of hOB cultured in contact with 3D scaffolds ($n = 5$) was evaluated as described in the literature [39,40]. Briefly, hOB cells were cultured in the presence of the scaffolds for 1 and 3 days (as described in Section 2.2.9.1). At predetermined intervals, the cells were lysed with Triton X-100 (1 % (v/v), 1 mL), then the cell-scaffold constructs were removed using a cell scraper and the remaining solution was transferred into eppendorfs. Afterward, the samples were subjected to a freeze-thaw cycle and sonicated for 15 min to further promote the cellular lysis. Subsequently, the samples were centrifuged (14,000 *g*, 15 min, at RT) and the ALP activity was determined by incubating 20 µL of the samples' supernatant with 60 µL of a substrate solution (0.2 % *p*-Nitrophenylphosphate (pNPP) (w/v) in 1 M diethanolamine HCl, at pH 9.8) at 37 °C, in the dark. After 45 min, the reaction was stopped with 80 µL of the stop solution (NaOH (2 M) containing EDTA (0.2 mM)). Then, the production of *p*-nitrophenol was evaluated by measuring the absorbance at 405 nm using a Biorad xMark microplate spectrophotometer. The ALP activity was determined according to the protocol provided by the manufacturer.

2.2.10. Statistical analysis

The results were statistically analyzed using one-way analysis of variance (ANOVA). A *p*-value lower than 0.05 ($p < 0.05$) was considered statistically significant.

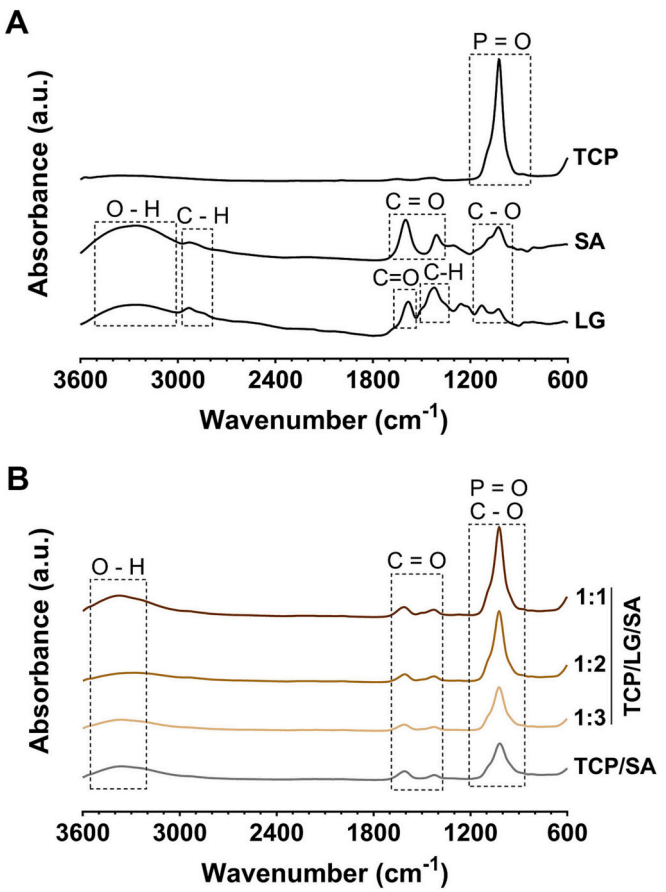

Fig. 2. ATR-FTIR analysis of TCP, SA, LG (A) and TCP/LG/SA_1:3, TCP/LG/SA_1:2, TCP/LG/SA_1:1, and TCP/SA scaffolds (B).

3. Results and discussion

3.1. Morphological characterization of the scaffolds

The 3D scaffolds were produced *via* the layer-by-layer deposition of the TCP, SA, and LG mixture using the Fab@Home 3D printer. The composition of the 3D printed mixture was chosen for mimicking the natural bone matrix composition (20–30 % organic, 70–80 % inorganic) [31,36]. The TCP was selected to mimic the inorganic phase, as well as confer the mechanical and osteogenic properties to the scaffolds. Otherwise, SA due to its polymeric nature, biocompatibility, and biodegradability, was used to mimic the bone organic phase. In addition, LG was also incorporated in this phase for further increment the mechanical properties of the scaffolds. The macroscopic images (Fig. 1A) show that the introduction of LG induces changes in the 3D scaffolds' color, from white to light brown, being darker in the TCP/LG/SA_1:1 scaffolds due to higher LG content. Nevertheless, all the formulations presented similar dimensions, designs, and shapes. Additionally, the scaffolds' surface morphology was further characterized by SEM (Fig. 1B). The SEM images show that the TCP/LG/SA and TCP/SA scaffolds present a similar irregular and rough surface. Such characteristics have been associated with enhanced bioactivity due to the higher number of anchorage points, that can promote protein adsorption and, subsequently, cell adhesion. Moreover, in previous studies reported in the literature, rough and irregular surfaces have been described as leading to higher production of extracellular matrix components as well as an increase in the metabolism of human osteoblast cells [41–43].

Table 2
EDS analysis of the 3D printed scaffolds.

	Elements ([a]wt.%)					
Sample	C	O	Na	P	Cl	Ca
TCP/LG/SA_1:3	11.23 ± 4.01	43.47 ± 11.99	0.19 ± 0.09	10.68 ± 0.91	2.80 ± 0.26	31.63 ± 1.97
TCP/LG/SA_1:2	13.47 ± 4.71	43.58 ± 12.37	0.17 ± 0.09	9.06 ± 0.82	3.16 ± 0.29	30.57 ± 2.01
TCP/LG/SA_1:1	16.04 ± 5.53	46.03 ± 13.29	0.16 ± 0.08	8.81 ± 0.83	2.52 ± 0.25	26.44 ± 1.80
TCP/SA	11.64 ± 4.57	45.86 ± 14.09	0.16 ± 0.09	8.97 ± 0.88	2.99 ± 0.30	30.37 ± 2.17

[a] wt.% - weight percentage.

3.2. Characterization of the scaffolds' physicochemical properties

3.2.1. ATR-FTIR analysis

The chemical composition of the 3D scaffolds was analyzed by ATR-FTIR (Fig. 2). The raw materials spectra show that the TCP exhibits a single characteristic peak at 1020 cm^{-1}, attributed to the P═O vibration. Moreover, in the SA spectra were identified two peaks at 1400 and 1600 cm^{-1}, corresponding to the C═O stretching of the carboxylate group, a band between 3000 and 3600 cm^{-1}, due to the OH groups of the alginate's G and M units, and vibration bands at 2930–2845 cm^{-1}, attributed to the C—H bonds. The LG's spectrum also shows a broad peak between 3000 and 3600 cm^{-1} that corresponds to OH groups and two peaks at 1131 and 1026 cm^{-1} attributed to the C—O bonds. Additionally, the LG also displays peaks at 2933 and 1583 cm^{-1} relating to the C—H and C═O stretch vibrations, respectively. Regarding the TCP/LG/SA and TCP/SA 3D scaffolds it is possible to observe the presence of the major peaks of each raw material. The TCP/SA shows the peaks at 3000–3600 cm^{-1}, 1131–1026 cm^{-1}, and 1020 cm^{-1} characteristics of TCP and SA materials, confirming the presence of raw materials in the scaffolds' composition. Similar data were obtained for TCP/LG/SA scaffolds, being observed the characteristic peaks for TCP, SA, and LG materials.

3.2.2. Energy dispersive spectroscopy analysis

The scaffolds' composition was further characterized *via* EDS analysis (Table 2). Compared to the TCP/SA scaffolds, the TCP/LG/SA_1:2 and TCP/LG/SA_1:1 scaffolds demonstrated a higher content of carbon and a lower amount of oxygen (Table 2). While TCP/SA scaffolds, in comparison to TCP/LG/SA_1:3, display a similar content of carbon and oxygen atoms. These differences can be explained by the higher LG content in the TCP/LG/SA_1:2 and TCP/LG/SA_1:1 scaffolds. Moreover, all formulations presented Ca/P ratios, in atomic % (Table S2), close to that observed in native trabecular bone, usually within the 1.3–2.2 range [44].

3.3. Characterization of the 3D scaffolds' mechanical properties

Scaffolds' mechanical stability is crucial for the bone regeneration process. Therefore, the scaffolds' mechanical properties are fundamental for their application in the bone regeneration process, acting as temporary replacements that maintain or improve bone tissue functions [45,46]. Moreover, the mechanical properties should be as close as possible to the bone tissue that needs replacement, for example, stiffer scaffolds can cause stress-shielding, whereas lower stiffnesses fail in providing mechanical stability to the lesion [47]. Herein, the mechanical properties (*i.e.*, compressive strength (*Cs*) and Young's modulus (*YM*)) of TCP/LG/SA_1:3, TCP/LG/SA_1:2, and TCP/LG/SA_1:1 scaffolds were compared against TCP/SA scaffolds, both in a dry and wet state (Fig. 3). The obtained results show that the scaffolds have higher *Cs* and *YM* in dry than in wet conditions. In a dry state, the TCP/LG/SA_1:3, TCP/LG/SA_1:2, TCP/LG/SA_1:1, and TCP/SA scaffolds presented *Cs* of ≈ 20, 21, 13, and 18 MPa, respectively. Such data shows that the LG

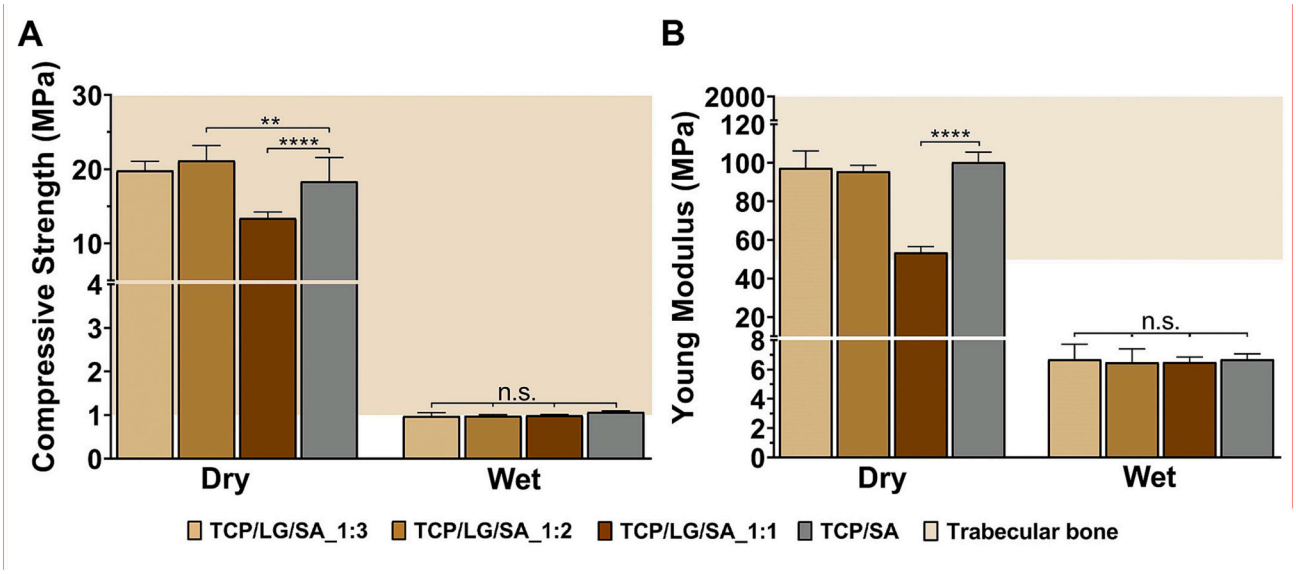

Fig. 3. Characterization of the 3D scaffolds' Cs (A) and YM (B), under dry and wet conditions. Data are presented as mean ± standard deviation, $n = 5$, $^{**}p < 0.01$ and $^{****}p < 0.0001$; n.s. – not statistically significant.

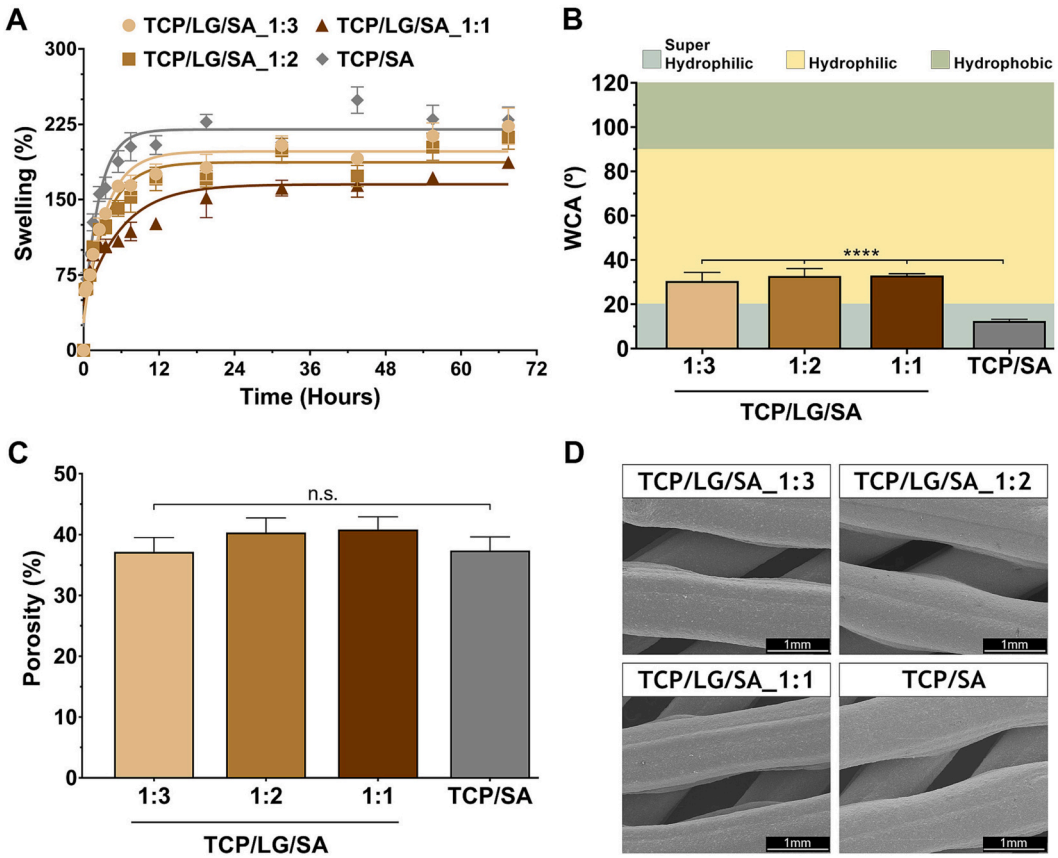

Fig. 4. Characterization of the 3D scaffolds' physicochemical properties. Analysis of the scaffolds' swelling profile (A); evaluation of the scaffolds' surface wettability (B); characterization of the scaffolds' total porosity (C); representative SEM images of the scaffolds' macroporosity (D). Data are presented as mean ± standard deviation, $n = 5$, $^{****}p < 0.0001$; n.s. - not statistically significant.

introduction can lead to stiffer materials, revealing an increase of 15 % in TCP/LG/SA_1:2 when compared to TCP/SA scaffolds. Moreover, the *Cs* values were within the upper range observed in native bone, *i.e.* 1–30 MPa [45,48–51]. In turn, these values significantly decreased for all the tested formulations in the wet state, presenting a *Cs* of ≈ 1 MPa.

Similarly, the TCP/LG/SA_1:3, TCP/LG/SA_1:2, and TCP/SA scaffolds, in the dry state, presented a *YM* value of ≈ 97, 96, 54, and 100 MPa, which are closer to those observed in native trabecular bone (50–2000 MPa) [45,48–51]. Furthermore, in wet conditions, these values significantly decreased to ≈ 7 MPa. In fact, the incorporation of

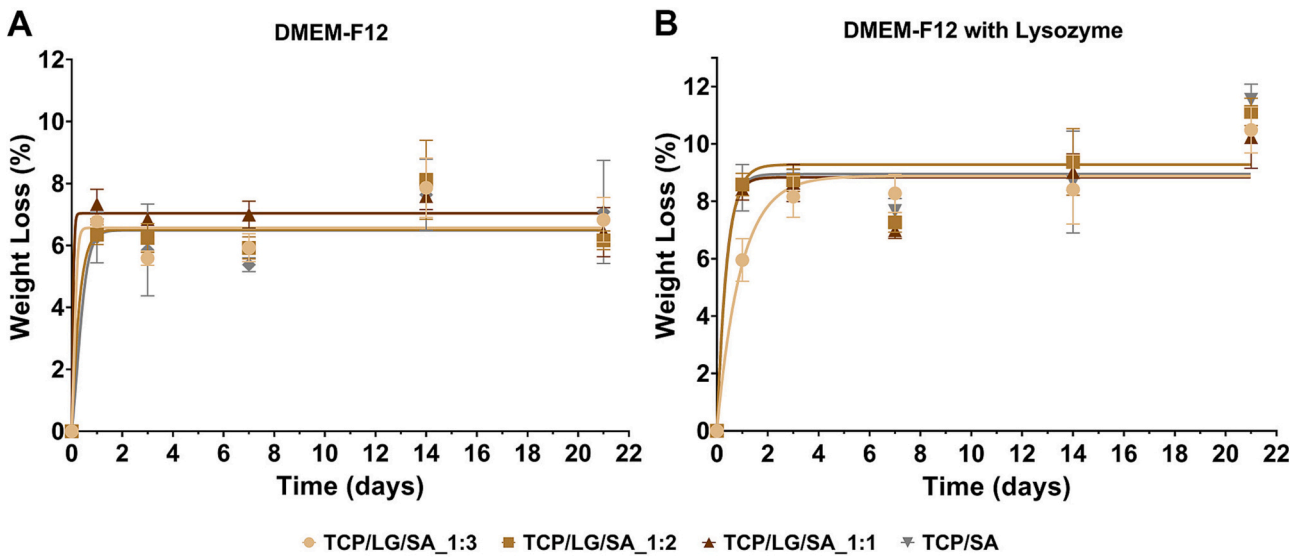

Fig. 5. Evaluation of the 3D scaffolds' weight loss over time in the absence (A) or presence (B) of lysozyme. Results are presented as mean ± standard deviation, $n = 5$.

LG is further supported when compared with other works available in the literature [37,52]. Boga and colleagues developed a TCP/alginic acid 3D scaffold (80/20 ratio) that presented increased brittleness with a *Cs* of 8 MPa (dry) and *YM* of 69 MPa (dry) [37]. Moreover, Castilho et al. also described the production of TCP/alginate 3D scaffolds using a powder printing technique. However, the produced scaffolds showed a maximum *Cs* of 20 MPa [52].

Altogether, these data show that the LG increases the mechanical resistance of the TCP/SA 3D scaffolds, presenting *Cs* and *YM* values within the range of trabecular bone. In this way, the TCP/LG/SA scaffolds should be applied to lesions in low load-bearing bones.

3.4. Evaluation of the 3D scaffolds' swelling profile

Scaffolds' swelling capacity is essential for their application in bone regeneration. The swelling can induce changes in the structure and size of the scaffolds, directly affecting their biological performance. For example, a high swelling capacity often results in the expansion of the polymeric matrix, which can mediate the increase of the scaffolds' pore size and therefore facilitate the cells' penetration and adhesion as well as the diffusion of molecules along the scaffolds' structure. However, excessive swelling may induce the loss of the scaffolds' mechanical integrity and also induce compressive stress in the surrounding tissue [53].

The swelling of the 3D scaffolds was investigated in TBS, for ≈ 3 days (Fig. 4A). The four formulations exhibited a similar swelling profile, with a fast abrupt swelling in the first 7.5 h, followed by a plateau phase (Fig. 4A). However, the TCP/SA scaffolds showed a higher swelling than their TCP/LG/SA counterparts. These results are attributed to the higher content of hydrophilic SA in TCP/SA formulations. In turn, the TCP/LG/SA formulation with a higher amount of hydrophobic LG, the TCP/LG/SA_1:1, showed a lower swelling during the experiment.

3.5. Determination of the 3D scaffolds' wettability

The scaffolds' wettability was evaluated by measuring the WCA at the materials' surface [54,55]. The hydrophilicity can affect both protein adsorption and cell adhesion. In the literature, it is reported that cell adhesion is favored on surfaces displaying a moderate hydrophilic character ($40° < WCA < 70°$), when compared with hydrophobic ($WCA > 90°$) or super hydrophilic surfaces ($WCA < 20°$) [56,57].

The results revealed that scaffolds TCP/SA exhibit a WCA value of ≈ 13°, demonstrating a super hydrophilic character (Fig. 4B). However, highly hydrophilic surfaces limit or completely impair cellular attachment and spreading. In fact, cell adhesion mediating molecules interact weakly with super hydrophilic surfaces [56]. In turn, the inclusion of the more hydrophobic LG changed the scaffolds' wettability, with a WCA value of ≈ 31° for TCP/LG/SA_1:3 and ≈ 33° for TCP/LG/SA_1:2 and TCP/LG/SA_1:1 scaffolds (Fig. 4B). Therefore, the LG incorporation resulted in scaffolds with a wettability closer to that considered ideal for biological applications. Such results are in accordance with other works reported in the literature that included LG in the scaffolds formulation. Mohammadalipour et al. observed that the addition of LG to polyhydroxybutyrate electrospun scaffolds enhanced the observed wettability, resulting in scaffolds with a moderate hydrophilic character WCA of 73° [27].

3.6. Evaluation of scaffolds' porosity

Scaffolds' porosity (*i.e.*, overall porosity, pore size, and pore interconnectivity) has a remarkable effect on cells' infiltration, proliferation, and growth. The pore size is essential to modulate the cells' movement to the interior regions of the scaffolds. Moreover, the interconnected pores can also facilitate the diffusion of different agents throughout the scaffolds, such as the Ca^{2+} and PO_4^{3-} ions allowing the formation of a hydroxyapatite-like layer [58].

The total porosity of the scaffolds was measured using the liquid displacement method (Fig. 4C). All the formulations presented a total porosity of 37–41 %, slightly lower than the ideal for trabecular bone (50–90 %) [59]. However, it is worth noticing that highly porous scaffolds may present sub-optimal mechanical strength due to their lower density. Furthermore, SEM images showed a macroporosity (1650 ± 250 μm × 650 ± 150 μm) compatible with cells' infiltration, new vessels' ingrowth, as well as promoting an adequate exchange of gases and nutrients (Fig. 4D). Additionally, the obtained porosity values are similar to those previously reported in the literature for different ceramic/polymer scaffolds. Boga and co-workers observed that the 3D printed TCP/alginic acid scaffolds at a ratio of 80/20, 70/30, and 60/40 presented an overall porosity of 50 %, 41 %, and 28 %, respectively [37]. Similarly, Diao et al. reported an overall porosity ranging from 38.25 to 63.78 % for 3D printed TCP scaffolds [60].

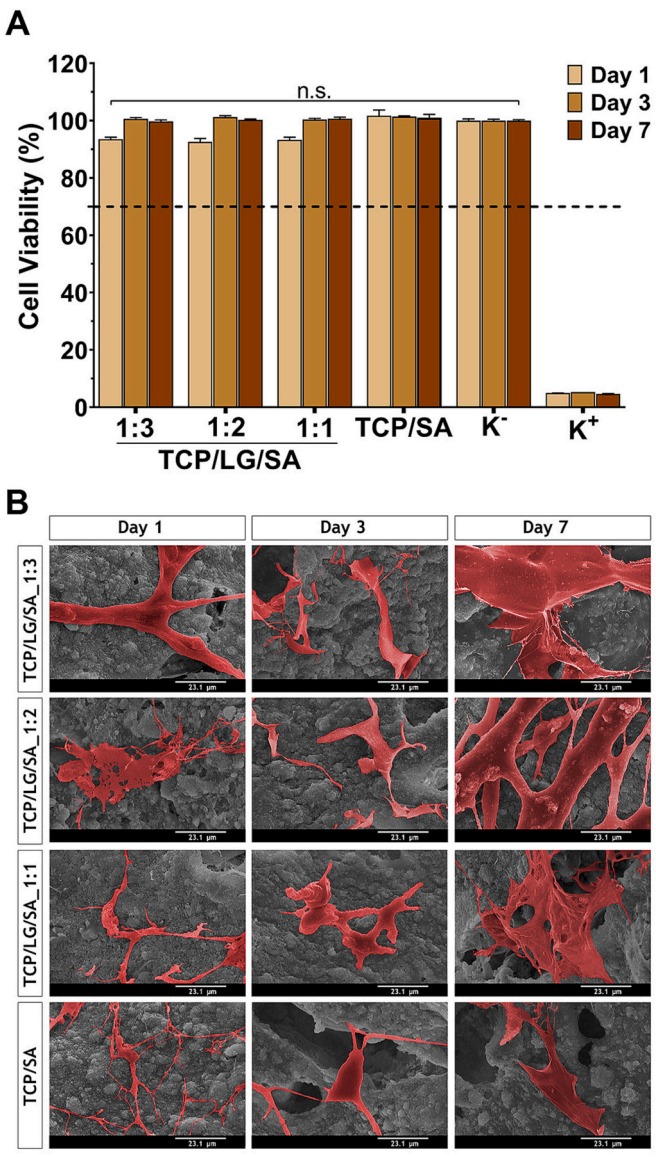

Fig. 6. Characterization of the scaffolds' cytocompatibility. Analysis of the cellular viability profile of hOB incubated in the presence of the 3D scaffolds through the resazurin assay at 1, 3, and 7 days. Cells incubated with ethanol were used as positive control (K+), whereas cells cultured without the scaffolds were used as the negative control (K-). Data are presented as the mean ± standard deviation, $n = 5$; n.s. - not statistically significant (A). Representative pseudo-colored SEM images of hOB cells seeded on the surface of 3D scaffolds for 1, 3, and 7 days. Scale bars represent 21.3 μm (B).

3.7. Characterization of scaffolds' biodegradation profile

The biodegradation profile is fundamental for assessing the application of 3D scaffolds as temporary supports for enhancing the bone regeneration process [61]. In this regard, the scaffolds' degradation rate must be proportional to the rate of new bone formation, without compromising the stability of the construct or the integrity of the tissue at the injured site. For that purpose, the 3D scaffolds' degradation profile was evaluated in DMEM-F12 in the absence or presence of lysozyme, an enzyme found in saliva, granules of neutrophils, macrophages, and serum (Fig. 5). The obtained results show that in the absence of lysozyme all formulations presented a maximum of ≈ 8 % weight loss, after 21 days. In the same period, in the presence of lysozyme, the total weight loss of the scaffolds increased to ≈ 12 %. Such can be justified by the lack of specificity of lysozyme towards SA and LG. In fact, the SA is mainly degraded *in vivo* by alginate lyases, whereas the LG can be slowly broken down by β-etherases [62,63]. Cheng and colleagues also reported a slow degradation profile of PLGA/β-TCP 3D scaffolds, reaching a total weight loss of 2.2 %, after 30 days [64]. In turn, Cabral and coworkers demonstrated that TCP/gelatin/chitosan scaffolds are degraded at a higher rate in the presence of lysozyme, which can degrade the chitosan, reaching a 20 % total weight loss after 21 days of incubation [38]. Therefore, the slower degradation profile observed for the TCP/LG/SA scaffolds can be explained by the lack of enzymes specific to LG and/or SA.

3.8. Characterization of the biological properties of the produced scaffolds

3.8.1. Evaluation of scaffolds' cytotoxic profile

The cytotoxic profile of the produced scaffolds and their degradation products was evaluated using the resazurin assay. hOB cells were used as a cell model to perform these assays. The obtained results revealed that hOB cells remained viable when in contact with the scaffolds for 7 days (Fig. 6A). Otherwise, SEM analysis clearly shows the cells' adhesion and spreading at the scaffolds' surface. Additionally, after 7 days, the increase in the cell density led to the establishment of several contact points between cells and maintained the typical osteoblastic morphology (Fig. 6B). These results were also corroborated by the live/dead staining confocal experiments (Fig. S1C) using Calcein-AM to label live cells and PI to identify dead cells. The hOB seeded in contact with both TCP/LG/SA and TCP/SA scaffolds showed a cell density similar to the K^- group, with very few PI-stained cells. Moreover, it is also possible to observe the hOB proliferation from day 1 to 3, which is essential for promoting the formation of new bone tissue. Such data is in accordance with the safety profile described in the literature for materials based on TCP, SA, and LG or even their combination [27,36,52]. Therefore, the obtained results demonstrate that the LG addition does not compromise the biological properties of these structures.

3.8.2. In vitro evaluation of the scaffolds' biomineralization

The 3D scaffolds' ability to promote/support the deposition of minerals is an important step for promoting the full regeneration of the bone. Particularly, the fixation of PO_4^{-3} and Ca^{2+} contributes to the formation of calcium phosphate crystals, namely in the form of hydroxyapatite ($Ca_5(PO_4)_3(OH)$) [65]. Thus, the scaffolds' mineralization upon incubation in SBF was evaluated over a period of 21 days. For this purpose, the formation of apatite crystals on the scaffolds' surface was monitored through SEM (Fig. 7A). The SEM images demonstrate the initial deposition of hydroxyapatite nanocrystals that continued to grow and formed plates at all the 3D scaffolds formulations with the progression of the incubation time. Additionally, the EDS analysis of the samples (Fig. S1A) indicates an increase in the ratio between the Calcium and Carbon content in the scaffolds, from day 7 to 21, further corroborating the deposition and maturation of hydroxyapatite at the scaffolds' surface.

Furthermore, the ARS staining evaluated the scaffolds' matrix mineralization when in the presence of hOB cells for 1, 3, 7, and 14 days (Fig. 7B). The obtained results also demonstrate that the LG addition does not compromise the scaffolds' biological performance. In fact, at all time points the TCP/LG/SA_1:3, TCP/LG/SA_1:2, TCP/LG/SA_1:1 scaffolds showed a similar ARS concentration to that obtained in TCP/SA scaffolds. In summary, the osteogenic properties can be mainly attributed to the TCP's intrinsic capacity to stimulate biomineralization, and consequently, facilitate the osteointegration of the 3D scaffolds [66,67]. Moreover, this enhanced biomineralization of TCP/LG/SA and TCP/SA scaffolds is in agreement with other reports available in the literature where similar polymer/ceramic matrices were used for bone tissue regeneration [31,36]. Wang et al. produced LG/PCL nanofibers and observed that these structures could mediate the formation of HAp crystals and consequent biomineralization [68]. Moreover, Boga and colleagues also reported that TCP/alginic acid 3D printed scaffolds act as

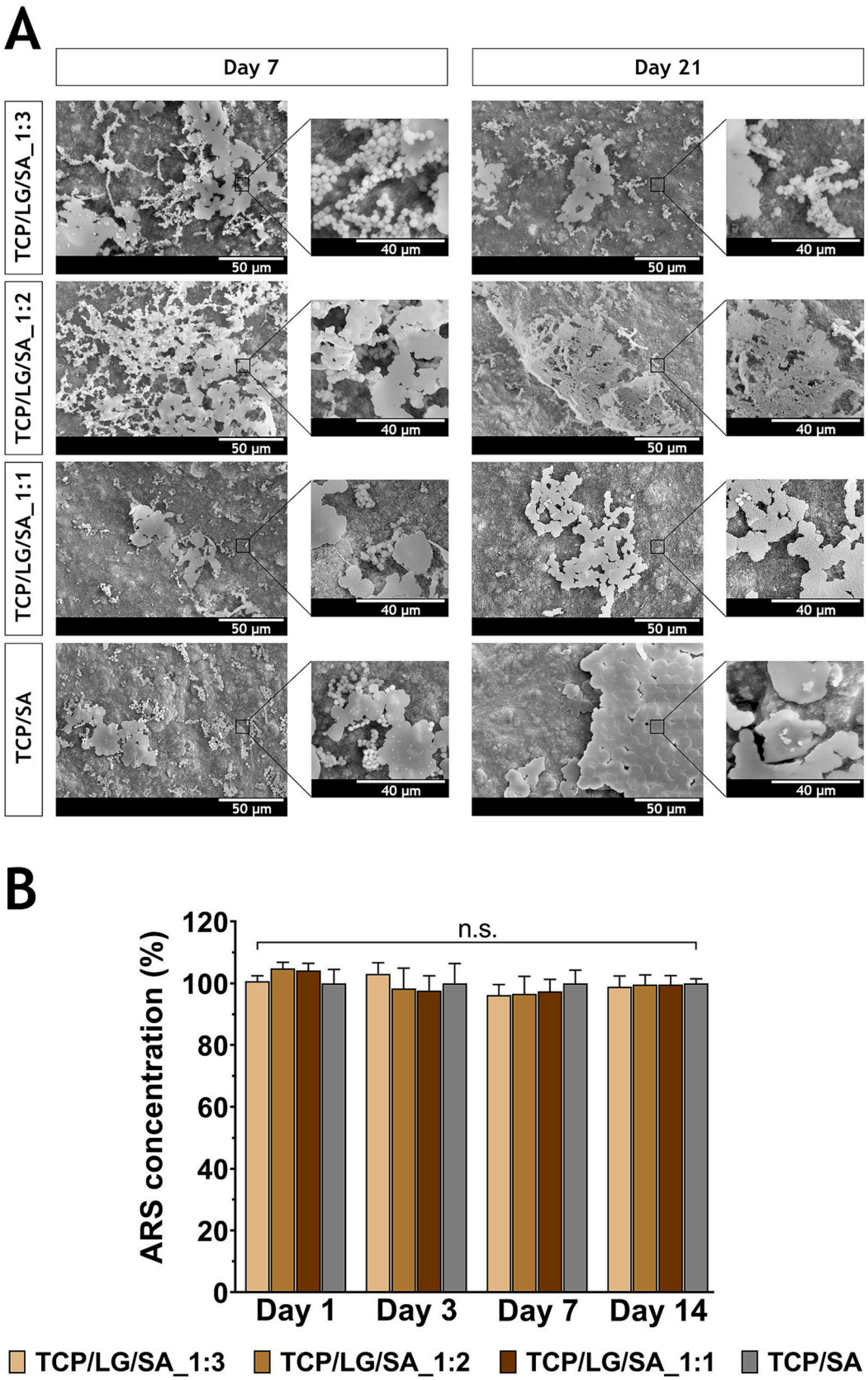

Fig. 7. Characterization of the scaffolds' biomineralization. Representative SEM images of the apatite deposition on the surface of TCP/LG/SA_1:3, TCP/LG/SA_1:2, TCP/LG/SA_1:1, and TCP/SA scaffolds (A). Analysis of the ARS concentration after 3D scaffolds incubation in the presence of hOB cells for 1, 3, 7, and 14 days. Data are presented as the mean ± standard deviation, $n = 6$; n.s. - not statistically significant (B).

supports for the mineral deposition leading to the formation of HAp crystals during 21 days [37]. Additionally, the characterization of the ALP activity of hOB cells seeded with TCP/LG/SA and TCP/SA scaffolds showed a slight increase, from 4.12 mU/mL in the control group to 4.6–5.4 mU/mL in cells seeded with the scaffolds (Fig. S1B). Such results further confirm the previous mineralization data and support the osteogenic potential of the TCP/LG/SA scaffolds.

4. Conclusion

Lignin mechanical and antioxidant properties coupled with a good biocompatibility profile have been supporting the development of lignin-based materials for biomedical applications, including tissue regeneration. In this work, a new 3D scaffold was produced, based on the TCP/LG/SA combination and layer-by-layer extrusion using a Fab@Home 3D plotter. The results demonstrated that the LG incorporation improved the mechanical resistance of the scaffolds, particularly the TCP/LG/SA_1:2 scaffolds showed a ≈ 15 % increase in the *Cs*. Moreover, it was also observed an increase in the WCA of the TCP/LG/SA scaffolds, presenting values closer to that considered ideal for biological applications. The mineralization potential was confirmed by the formation of HAp crystals and plates at the surface of the scaffolds and the ALP activity showed by hOB cells. Furthermore, TCP/LG/SA scaffolds presented an higher cytocompatibility, which was further confirmed by the confocal live/dead experiments and SEM images of the hOB cells adhesion and proliferation. Altogether, the results support the incorporation of LG in the 3D scaffolds for bone regeneration, originating stronger structures with more suitable environments for cell adhesion and proliferation. Moreover, it is worth noticing, that to the best of our knowledge, this is one of the first works exploring the LG application to reinforce TCP/SA scaffolds. In the future, osteopontin, osteocalcin, and BMP-2 expression assays should be performed to further characterize the osteoinductive and osteoconductive properties of TCP/LG/SA scaffolds. Moreover, the introduction of stem cells and/or bioactive molecules (*e.g.*, growth factors and bone morphogenic proteins) in the TCP/LG/SA mixture before the printing process may be pursued to enhance the 3D scaffolds' functionality and impact on the bone healing process. Following that, the evaluation *in vivo* of the performance of TCP/LG/SA scaffolds will be essential to validate their potential for bone healing applications.

CRediT authorship contribution statement

A.S. Silva-Barroso: Conceptualization, Methodology, Investigation, Writing - Original Draft. Cátia S. D. Cabral: Conceptualization, Methodology, Investigation, Writing - Original Draft. Paula Ferreira: Investigation, Writing - Original Draft. André F. Moreira: Conceptualization, Methodology, Investigation, Writing - Original Draft, Writing- Reviewing and Editing. Ilídio J. Correia: Conceptualization, Writing- Reviewing and Editing, Funding acquisition.

Declaration of competing interest

The authors declare that they have no known competing financial interests or personal relationships that could have appeared to influence the work reported in this paper.

Data availability

Data will be made available on request.

Acknowledgments

The authors would like to acknowledge Abílio Silva for the help in the mechanical assays. This work was financed by the Foundation for Science and Technology (FCT), through funds from the State Budget, and by the European Regional Development Fund (ERDF), under the Portugal 2020 Program, through the Regional Operational Program of the Center (Centro2020), through the Project with the reference UIDB/00709/2020. The funding from CENTRO-01-0145-FEDER-028989 and POCI-01-0145-FEDER-031462 are also acknowledged. Cátia S. D. Cabral is recipient of a doctoral fellowship from FCT (UI/BD/151024/2021) under the scope of the CICS-UBI Programmatic Funding (UIDP/00709/2020).

Appendix A. Supplementary data

Supplementary data to this article can be found online at https://doi.org/10.1016/j.ijbiomac.2023.124258.

References

[1] G. Zhu, T. Zhang, M. Chen, K. Yao, X. Huang, B. Zhang, Y. Li, J. Liu, Y. Wang, Z. Zhao, Bone physiological microenvironment and healing mechanism: basis for future bone-tissue engineering scaffolds, Bioact.Mater. 6 (11) (2021) 4110–4140.
[2] N. Su, J. Yang, Y. Xie, X. Du, H. Chen, H. Zhou, L. Chen, Bone function, dysfunction and its role in diseases including critical illness, Int. J. Biol. Sci. 15 (4) (2019) 776–787.
[3] E.F. Morgan, G.L. Barnes, T.A. Einhorn, Chapter 1 - the bone organ system: form and function, in: R. Marcus, D. Feldman, D.W. Dempster, M. Luckey, J.A. Cauley (Eds.), Osteoporosis (Fourth Edition), Academic Press, San Diego, 2013, pp. 3–20.
[4] W. Wang, K.W.K. Yeung, Bone grafts and biomaterials substitutes for bone defect repair: a review, Bioact.Mater. 2 (4) (2017) 224–247.
[5] V. Campana, G. Milano, E. Pagano, M. Barba, C. Cicione, G. Salonna, W. Lattanzi, G. Logroscino, Bone substitutes in orthopaedic surgery: from basic science to clinical practice, J. Mater. Sci. Mater. Med. 25 (10) (2014) 2445–2461.
[6] H.J. Haugen, S.P. Lyngstadaas, F. Rossi, G. Perale, Bone grafts: which is the ideal biomaterial? J. Clin. Periodontol. 46 (2019) 92–102.
[7] L.-Y. Zhang, Q. Bi, C. Zhao, J.-Y. Chen, M.-H. Cai, X.-Y. Chen, Recent advances in biomaterials for the treatment of bone defects, Organogenesis 16 (4) (2020) 113–125.
[8] M.N. Collins, G. Ren, K. Young, S. Pina, R.L. Reis, J.M. Oliveira, Scaffold fabrication technologies and structure/function properties in bone tissue engineering, Adv. Funct. Mater. 31 (21) (2021), 2010609.
[9] C.A. Murphy, A.K. Garg, J. Silva-Correia, R.L. Reis, J.M. Oliveira, M.N. Collins, The meniscus in normal and osteoarthritic tissues: facing the structure property challenges and current treatment trends, Annu. Rev. Biomed. Eng. 21 (1) (2019) 495–521.
[10] S.V. Lopes, M.N. Collins, R.L. Reis, J.M. Oliveira, J. Silva-Correia, Vascularization approaches in tissue engineering: recent developments on evaluation tests and modulation, ACS Appl.Bio Mater. 4 (4) (2021) 2941–2956.
[11] B. Yuan, S.-Y. Zhou, X.-S. Chen, Rapid prototyping technology and its application in bone tissue engineering, J.Zhejiang Univ.-Sci.B 18 (4) (2017) 303–315.
[12] A.R. Amini, C.T. Laurencin, S.P. Nukavarapu, Bone tissue engineering: recent advances and challenges, Crit. Rev. Biomed. Eng. 40 (5) (2012) 363–408.
[13] R. Florencio-Silva, G.R.d.S. Sasso, E. Sasso-Cerri, M.J. Simões, P.S. Cerri, Biology of bone tissue: structure, function, and factors that influence bone cells, BioMed Res. Int. 2015 (2015).
[14] X. Lin, S. Patil, Y.-G. Gao, A. Qian, The bone extracellular matrix in bone formation and regeneration, Front. Pharmacol. 11 (2020) 757.
[15] P. Chocholata, V. Kulda, V. Babuska, Fabrication of scaffolds for bone-tissue regeneration, Materials 12 (4) (2019) 568.
[16] M.S.B. Reddy, D. Ponnamma, R. Choudhary, K.K. Sadasivuni, A comparative review of natural and synthetic biopolymer composite scaffolds, Polymers 13 (7) (2021) 1105.
[17] M.R. Cohn, A. Unnanuntana, T.J. Pannu, S.J. Warner, J.M. Lane, 7.16 materials in fracture fixation, in: P. Ducheyne (Ed.), Comprehensive Biomaterials II, Elsevier, Oxford, 2017, pp. 278–297.
[18] B. Huang, G. Caetano, C. Vyas, J.J. Blaker, C. Diver, P. Bártolo, Polymer-ceramic composite scaffolds: the effect of hydroxyapatite and β-tri-calcium phosphate, Materials 11 (1) (2018) 129.
[19] L.A. Loureiro dos Santos, Natural Polymeric Biomaterials: Processing and Properties, Reference Module in Materials Science and Materials Engineering, Elsevier, 2017.
[20] F. Liu, Q. Chen, C. Liu, Q. Ao, X. Tian, J. Fan, H. Tong, X. Wang, Natural polymers for organ 3D bioprinting, Polymers 10 (11) (2018) 1278.
[21] A. Ahmad, N. Mubarak, F.T. Jannat, T. Ashfaq, C. Santulli, M. Rizwan, A. Najda, M. Bin-Jumah, M.M. Abdel-Daim, S. Hussain, A critical review on the synthesis of natural sodium alginate based composite materials: an innovative biological polymer for biomedical delivery applications, Processes 9 (1) (2021) 137.
[22] M.S. Ganewatta, H.N. Lokupitiya, C. Tang, Lignin biopolymers in the age of controlled polymerization, Polymers 11 (7) (2019) 1176.
[23] Q. Liu, L. Luo, L. Zheng, Lignins: biosynthesis and biological functions in plants, Int. J. Mol. Sci. 19 (2) (2018) 335.
[24] R.A. Dixon, J. Barros, Lignin biosynthesis: old roads revisited and new roads explored, Open Biol. 9 (12) (2019), 190215.

[25] S. Sugiarto, Y. Leow, C.L. Tan, G. Wang, D. Kai, How far is lignin from being a biomedical material? Bioact.Mater. 8 (2022) 71–94.
[26] R. Kumar, A. Butreddy, N. Kommineni, P.G. Reddy, N. Bunekar, C. Sarkar, S. Dutt, V.K. Mishra, K.R. Aadil, Y.K. Mishra, Lignin: drug/gene delivery and tissue engineering applications, Int. J. Nanomedicine 16 (2021) 2419–2441.
[27] M. Mohammadalipour, T. Behzad, S. Karbasi, Z. Mohammadalipour, Optimization and characterization of polyhydroxybutyrate/lignin electro-spun scaffolds for tissue engineering applications, Int. J. Biol. Macromol. 218 (2022) 317–334.
[28] P. Rejmontová, A. Kovalcik, P. Humpolíček, Z. Capáková, E. Wrzecionko, P. Sáha, The use of fractionated kraft lignin to improve the mechanical and biological properties of PVA-based scaffolds, RSC Adv. 9 (22) (2019) 12346–12353.
[29] R. Eivazzadeh-Keihan, E. Zare-Bakheir, H.A.M. Aliabadi, M.G. Gorab, H. Ghafuri, A. Maleki, H. Madanchi, M. Mahdavi, A novel, bioactive and antibacterial scaffold based on functionalized graphene oxide with lignin, silk fibroin and ZnO nanoparticles, Sci. Rep. 12 (1) (2022) 8770.
[30] M. Witzler, A. Alzagameem, M. Bergs, B.E. Khaldi-Hansen, S.E. Klein, D. Hielscher, B. Kamm, J. Kreyenschmidt, E. Tobiasch, M. Schulze, Lignin-derived biomaterials for drug release and tissue engineering, Molecules 23 (8) (2018) 1885.
[31] T.R. Correia, D.R. Figueira, K.D. de Sá, S.P. Miguel, R.G. Fradique, A.G. Mendonça, I.J. Correia, 3D printed scaffolds with bactericidal activity aimed for bone tissue regeneration, Int. J. Biol. Macromol. 93 (2016) 1432–1445.
[32] T. Kokubo, H. Takadama, How useful is SBF in predicting in vivo bone bioactivity? Biomaterials 27 (15) (2006) 2907–2915.
[33] A. Torres, V. Gaspar, I. Serra, G. Diogo, R. Fradique, A. Silva, I. Correia, Bioactive polymeric–ceramic hybrid 3D scaffold for application in bone tissue regeneration, Mater. Sci. Eng. C 33 (7) (2013) 4460–4469.
[34] J. Valente, T.A.M. Valente, P. Alves, P. Ferreira, A. Silva, I. Correia, Alginate based scaffolds for bone tissue engineering, Mater. Sci. Eng. C 32 (8) (2012) 2596–2603.
[35] H. Jiankang, L. Dichen, L. Yaxiong, Y. Bo, L. Bingheng, L. Qin, Fabrication and characterization of chitosan/gelatin porous scaffolds with predefined internal microstructures, Polymer 48 (15) (2007) 4578–4588.
[36] R. Fradique, T.R. Correia, S. Miguel, K. De Sa, D. Figueira, A. Mendonça, I. Correia, Production of new 3D scaffolds for bone tissue regeneration by rapid prototyping, J. Mater. Sci. Mater. Med. 27 (4) (2016) 1–14.
[37] J.C. Boga, S.P. Miguel, D. de Melo-Diogo, A.G. Mendonça, R.O. Louro, I.J. Correia, In vitro characterization of 3D printed scaffolds aimed at bone tissue regeneration, Colloids Surf. B: Biointerfaces 165 (2018) 207–218.
[38] C.S.D. Cabral, S.P. Miguel, D. de Melo-Diogo, R.O. Louro, I.J. Correia, Green reduced graphene oxide functionalized 3D printed scaffolds for bone tissue regeneration, Carbon 146 (2019) 513–523.
[39] J.L. Moreau, H.H.K. Xu, Mesenchymal stem cell proliferation and differentiation on an injectable calcium phosphate – chitosan composite scaffold, Biomaterials 30 (14) (2009) 2675–2682.
[40] F. Ghorbani, B. Ghalandari, M. Sahranavard, A. Zamanian, M.N. Collins, Tuning the biomimetic behavior of hybrid scaffolds for bone tissue engineering through surface modifications and drug immobilization, Mater. Sci. Eng. C 130 (2021), 112434.
[41] Y. Du, J.L. Guo, J. Wang, A.G. Mikos, S. Zhang, Hierarchically designed bone scaffolds: from internal cues to external stimuli, Biomaterials 218 (2019), 119334.
[42] K. Rechendorff, M.B. Hovgaard, M. Foss, V. Zhdanov, F. Besenbacher, Enhancement of protein adsorption induced by surface roughness, Langmuir 22 (26) (2006) 10885–10888.
[43] A.R. Calore, V. Srinivas, L. Groenendijk, A. Serafim, I.C. Stancu, A. Wilbers, N. Leoné, A.A. Sanchez, D. Auhl, C. Mota, K. Bernaerts, J.A.W. Harings, L. Moroni, Manufacturing of scaffolds with interconnected internal open porosity and surface roughness, Acta Biomater. 156 (2022) 158–176.
[44] P. Sotiropoulou, G. Fountos, N. Martini, V. Koukou, C. Michail, I. Kandarakis, G. Nikiforidis, Bone calcium/phosphorus ratio determination using dual energy X-ray method, Phys.Med. 31 (3) (2015) 307–313.
[45] S. Bose, M. Roy, A. Bandyopadhyay, Recent advances in bone tissue engineering scaffolds, Trends Biotechnol. 30 (10) (2012) 546–554.
[46] C.F. Santos, A.P. Silva, L. Lopes, I. Pires, I.J. Correia, Design and production of sintered β-tricalcium phosphate 3D scaffolds for bone tissue regeneration, Mater. Sci. Eng. C 32 (5) (2012) 1293–1298.
[47] L. Bi, W. Cheng, H. Fan, G. Pei, Reconstruction of goat tibial defects using an injectable tricalcium phosphate/chitosan in combination with autologous platelet-rich plasma, Biomaterials 31 (12) (2010) 3201–3211.
[48] E.F. Morgan, G.U. Unnikrisnan, A.I. Hussein, Bone mechanical properties in healthy and diseased states, Annu. Rev. Biomed. Eng. 20 (2018) 119–143.
[49] X. Zhang, X.-W. Li, J.-G. Li, X.-D. Sun, Preparation and mechanical property of a novel 3D porous magnesium scaffold for bone tissue engineering, Mater. Sci. Eng. C 42 (2014) 362–367.
[50] L.-C. Gerhardt, A.R. Boccaccini, Bioactive glass and glass-ceramic scaffolds for bone tissue engineering, Materials 3 (7) (2010) 3867–3910.
[51] S. Mohamed, B.H. Shamaz, Bone tissue engineering and bony scaffolds, Int. J. Dent. Oral Health 1 (2015) 15–20.
[52] M. Castilho, J. Rodrigues, I. Pires, B. Gouveia, M. Pereira, C. Moseke, J. Groll, A. Ewald, E. Vorndran, Fabrication of individual alginate-TCP scaffolds for bone tissue engineering by means of powder printing, Biofabrication 7 (1) (2015), 015004.
[53] L. Tao, L. Zhonglong, X. Ming, Y. Zezheng, L. Zhiyuan, Z. Xiaojun, W. Jinwu, In vitro and in vivo studies of a gelatin/carboxymethyl chitosan/LAPONITE® composite scaffold for bone tissue engineering, RSC Adv. 7 (85) (2017) 54100–54110.
[54] G. Diogo, V. Gaspar, I. Serra, R. Fradique, I. Correia, Manufacture of β-TCP/alginate scaffolds through a Fab@ home model for application in bone tissue engineering, Biofabrication 6 (2) (2014), 025001.
[55] S. Guo, X. Zhu, M. Li, L. Shi, J.L.T. Ong, D. Jańczewski, K.G. Neoh, Parallel control over surface charge and wettability using polyelectrolyte architecture: effect on protein adsorption and cell adhesion, ACS Appl. Mater. Interfaces 8 (44) (2016) 30552–30563.
[56] S.M. Oliveira, N.M. Alves, J.F. Mano, Cell interactions with superhydrophilic and superhydrophobic surfaces, J. Adhes. Sci. Technol. 28 (8–9) (2014) 843–863.
[57] D.P. Dowling, I.S. Miller, M. Ardhaoui, W.M. Gallagher, Effect of surface wettability and topography on the adhesion of osteosarcoma cells on plasma-modified polystyrene, J. Biomater. Appl. 26 (3) (2011) 327–347.
[58] S.J. Hollister, Porous scaffold design for tissue engineering, Nat. Mater. 4 (7) (2005) 518–524.
[59] V. Karageorgiou, D. Kaplan, Porosity of 3D biomaterial scaffolds and osteogenesis, Biomaterials 26 (27) (2005) 5474–5491.
[60] J. Diao, J. OuYang, T. Deng, X. Liu, Y. Feng, N. Zhao, C. Mao, Y. Wang, 3D-plotted beta-tricalcium phosphate scaffolds with smaller pore sizes improve in vivo bone regeneration and biomechanical properties in a critical-sized calvarial defect rat model, Adv.Healthc.Mater. 7 (17) (2018), 1800441.
[61] F.J. O'Brien, Biomaterials & scaffolds for tissue engineering, Mater. Today 14 (3) (2011) 88–95.
[62] B. Zhu, H. Yin, Alginate lyase: review of major sources and classification, properties, structure-function analysis and applications, Bioengineered 6 (3) (2015) 125–131.
[63] P. Picart, P.D. de María, A. Schallmey, From gene to biorefinery: microbial β-etherases as promising biocatalysts for lignin valorization, Front. Microbiol. 6 (2015) 916.
[64] W.-X. Cheng, Y.-Z. Liu, X.-B. Meng, Z.-T. Zheng, L.-L. Li, L.-Q. Ke, L. Li, C.-S. Huang, G.-Y. Zhu, H.-D. Pan, L. Qin, X.-L. Wang, P. Zhang, PLGA/β-TCP composite scaffold incorporating cucurbitacin B promotes bone regeneration by inducing angiogenesis, J. Orthop. Transl. 31 (2021) 41–51.
[65] H.C. Blair, Q.C. Larrouture, Y. Li, H. Lin, D. Beer-Stoltz, L. Liu, R.S. Tuan, L. J. Robinson, P.H. Schlesinger, D.J. Nelson, Osteoblast differentiation and bone matrix formation in vivo and in vitro, Tissue Eng. B Rev. 23 (3) (2017) 268–280.
[66] W. Chu, Y. Gan, Y. Zhuang, X. Wang, J. Zhao, T. Tang, K. Dai, Mesenchymal stem cells and porous β-tricalcium phosphate composites prepared through stem cell screen-enrich-combine(−biomaterials) circulating system for the repair of critical size bone defects in goat tibia, Stem Cell Res. Ther. 9 (1) (2018) 157.
[67] H. Tebyanian, M.H. Norahan, H. Eyni, M. Movahedin, S.J. Mortazavi, A. Karami, M.R. Nourani, N. Baheiraei, Effects of collagen/β-tricalcium phosphate bone graft to regenerate bone in critically sized rabbit calvarial defects, J. Appl. Biomater. Funct. Mater. 17 (1) (2019), 2280800018820490.
[68] D. Wang, J. Jang, K. Kim, J. Kim, C.B. Park, "Tree to bone": lignin/polycaprolactone nanofibers for hydroxyapatite biomineralization, Biomacromolecules 20 (7) (2019) 2684–2693.